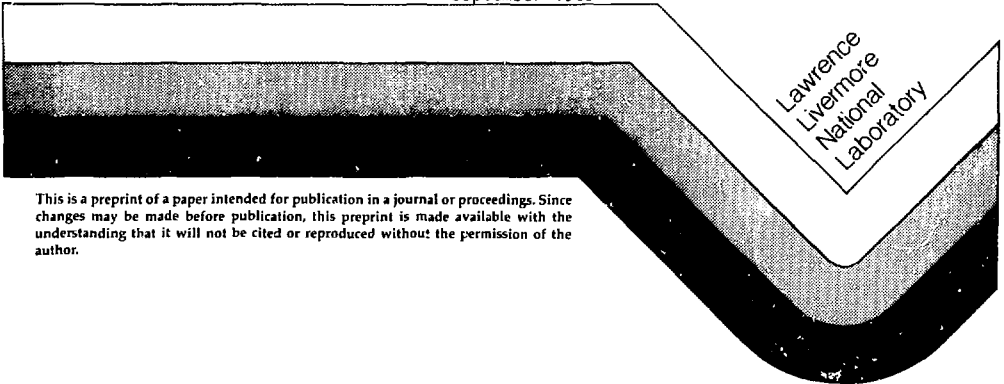


HIGH FREQUENCY ELECTROMAGNETIC TOMOGRAPHY

W. Daily  
A. Ramirez  
T. Uerg  
R. Latorre

This paper was prepared for submittal to  
Nuclear Waste Isolation in the Unsaturated Zone  
Las Vegas, Nevada, September 18-21, 1989

September 1989



This is a preprint of a paper intended for publication in a journal or proceedings. Since changes may be made before publication, this preprint is made available with the understanding that it will not be cited or reproduced without the permission of the author.

## DISCLAIMER

This document was prepared as an account of work sponsored by an agency of the United States Government. Neither the United States Government nor the University of California nor any of their employees, makes any warranty, express or implied, or assumes any legal liability or responsibility for the accuracy, completeness, or usefulness of any information, apparatus, product, or process disclosed, or represents that its use would not infringe privately owned rights. Reference herein to any specific commercial products, process, or service by trade name, trademark, manufacturer, or otherwise, does not necessarily constitute or imply its endorsement, recommendation, or favoring by the United States Government or the University of California. The views and opinions of authors expressed herein do not necessarily state or reflect those of the United States Government or the University of California, and shall not be used for advertising or product endorsement purposes.

Prepared by Yucca Mountain Project (YMP) participants as part of the Civilian Radioactive Waste Management Program. The Yucca Mountain Project is managed by the Waste Management Project Office of the U.S. Department of Energy, Nevada Operations Office. Yucca Mountain Project work is sponsored by the DOE Office of Civilian Radioactive Waste Management.

\*Work performed under the auspices of the U.S. Department of Energy by Lawrence Livermore National Laboratory under Contract W-7405-ENG-48.

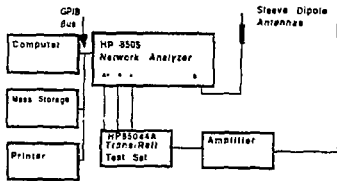


Figure 2. Block diagram of the high frequency electromagnetic (HFEM) system.

$$r \frac{1/2}{\epsilon_0} \Delta\psi \Delta\omega = C \Delta\psi \Delta\omega \quad (1)$$

where

$\Delta\psi$  = measured phase change

$\Delta\omega$  = angular frequency change (20 MHz)

$r$  = known ray path length

$\epsilon_r$  = the electromagnetic permittivity of the rock

$\epsilon_0$  = the electromagnetic permittivity of free space

$c$  = speed of light

we can obtain the line integral permittivity  $\epsilon^{1/2}$ , along each ray. Equation (1) is valid for a homogeneous medium in the far field of the transmitting antenna.

#### DATA ANALYSIS

Image reconstruction is by an algorithm described by Dines and Lytle.<sup>2</sup> The region in the plane between the boreholes is represented by the material parameter such as velocity  $v(x, y)$  or attenuation rate  $\alpha(x, y)$  which is to be calculated. Attenuation rate is a measure of how rapidly signal energy is dissipated with distance. However, work reported herein deals primarily with signal phase velocity, therefore we illustrate the analysis by writing the relation between it and total signal delay along the  $k$ th path  $R_k$

$$t_k = \int_{R_k} \frac{ds}{v(x, y)} \quad k = 1, 2, \dots, K \quad (2)$$

We want to reconstruct an image of the velocity function  $v(x, y)$  from line integral data  $t_k$  collected from  $K$  rays of Eq. (2). These are a set of  $K$  linear equations which can be solved for  $1/v(x, y)$ . Typically, Eq. (2) is converted to a discrete form by superimposing an  $I \times J$  grid on the image plane thus defining pixels so that the discretized  $1/v(x, y)$ , which we denote  $1/v_{ij}$ , can be assumed constant over each pixel. This approximation results in a system of  $K$  equations

in  $I \times J$  unknowns:

$$t_k = \sum_i \sum_j D_{s_{ij}} v_{ij} \quad k = 1, 2, \dots, K \quad (3)$$

where  $D_{s_{ij}}$  is the ray length of ray  $k$  through cell  $ij$  and it is understood that  $D_{s_{ij}} = 0$  for all  $i$  and  $j$  not intercepted by a ray. Solution of Eq. (3) poses several problems. First the data  $t_k$  are necessarily inexact because of data noise which generally will make Eq. (3) inconsistent. Second, the number of independent equations can be insufficient so that the equations are underdetermined. Third, usually the number of equations is too large to be solved by direct inversion methods.

Iterative methods, especially suitable for computer solutions, have been devised which work well on underdetermined and inconsistent data. We have used the simultaneous iterative reconstruction technique (SIRT). It begins with an initial guess of  $v_k$  and calculates an estimate for the data  $t_k$ . Then the difference between the data and calculated set is distributed along the ray paths. This leads to corrections in the estimated velocity function which, when applied, bring the estimate closer to the desired function. This process is repeated ray by ray and each cell is updated after all rays passing through a cell are considered. Ideally, these iterations continue until changes in the calculated  $t_k$  are of the order of the data noise. The algorithm is described in detail by Dines and Lytle.<sup>2</sup> The resultant image can then be smoothed using a linear interpolation algorithm which averages over an effective length of about one cell dimension but produces an image with 9 times the number of cells actually used in reconstruction.

#### MEASUREMENT PRECISION

Both systematic and random measurement errors occur from several sources. In this section two of these potential error sources are discussed and an estimate made as to their impact on the HFEM results.

**System Calibration.** The measurement system was calibrated by subtracing, point by point, two phase characteristics; one when the antennas were placed adjacent to each other and the other for the measurement through the rockmass. In the first case  $r=0$  in Eq. (1) and therefore the system reference delay was adjusted to force  $\Delta\psi = 0$  (see Eq. (1)). The difference between this phase characteristic and that measured through the rockmass provided a single calibration point for the system at  $r=0$ .

One source of error introduced into each tomograph by this calibration is the seemingly simple requirement that the antenna separation is indeed zero. (Actually, the requirement is that the separation be the same each time the calibration is performed. If it is not zero then the rockmass measurement of phase will be with respect to whatever separation is used. This fact works to our advantage because it allows removal of the

effects of the antenna casing [used to center the antennas in the boreholes] from the phase measurement.) This is a problem because both antennas are in a casing designed to help center the antenna in the borehole and to remove the impedance mismatch between the air in the hole and the rockmass. The antennas slip a small amount in the casing during the experiment. Therefore, during the calibration procedure, placing the antenna casings adjacent to each other where the antennas were presumed to be, did not guarantee that the antennas were aligned. We estimate that the alignment error could have been as much as a few centimeters. Tests that we performed show that this type of alignment error would result in a typical uncertainty in the value of  $\sqrt{\epsilon}$  for the rockmass of 2% but an error always less than 5%.

Another disadvantage with this calibration is that the phase change is measurable only relative to an unknown but constant value. This is because the antennas are electromagnetically loaded differently for calibration and for data acquisition with the result that each calculated permittivity is shifted some unknown but constant amount. Therefore the measured values of permittivity are relative only. However, the alterant tomographs, formed from differences in measured relative permittivity, contain reliable information on the changes in permittivity.

**Multipath signal propagation.** One of the objectives for the HFEM work is to evaluate the impact of high contrast anomalies (e.g., metallic heater canister or large diameter borehole) on the validity of the image reconstructions. Such anomalies can cause complex reflection and refraction of the waves, making the data difficult or impossible to interpret with the approximation of straight ray paths used by our inversion algorithm. Accurate determination of the effects of the heater would have required comparison of reconstructions from data sets taken before the heater hole was drilled and after it was drilled and the heater installed. However, other factors dictated that the heater hole was the first hole drilled. Therefore, our test for effects of interference from the heater had to be a comparison of reconstructions with the heater in place and with it removed. This test showed that reconstructions in the image planes between Ne2a and Ne1, Ne3 and Ne4 (9.5 to 11.5 m) and between Ne4 and Ne5 (9.5 to 11.5 m) were least affected by scattering from the heater. In fact, in the half of each of these image planes furthest from the end of the heater (see Fig. 1), the effect was to change the pixel values of  $\sqrt{\epsilon}$  by less than 0.15

#### DATA INTERPRETATION

The tomographs generated in this work are of electromagnetic permittivity of the rockmass. Of course, images of this parameter by itself are of little help in determining the near field environment of the canister. To be useful electromagnetic permittivity must be interpretable in terms of water content in the rock, because this is the property that has a bearing on the canister survivability.

A quantitative interpretation requires laboratory calibration of the electromagnetic properties of densely welded tuff; that is, measurement of their dielectric properties as a function of water content and temperature. This calibration then allows inference of *in situ* water content from tomographic dielectric

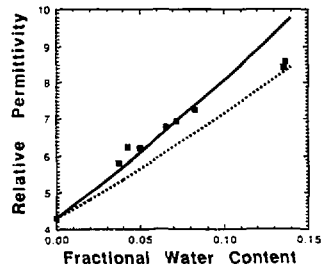


**Figure 3.** Laboratory measured and model calculations of the relative permittivity as a function of water content. The points are laboratory measurement of the electromagnetic permittivity (real part) of densely welded, Grouse canyon tuff of porosity 0.14. Reflection and transmission coefficients measured in a coaxial air line at 200 MHz were used to calculate the permittivity. Water from well J-13 was used as the pore fluid. The solid line is the relative permittivity as a function of water content for a multiphase dielectric mixture model. Spherical inclusions of air ( $\epsilon_r = 1$ ) and thin needle inclusions of water ( $\epsilon_r = 81$ ) are dispersed in a background of silicate material ( $\epsilon_r = 5$ ) of total porosity 0.14. The dashed line is for the same model but with a water permittivity of 56 which is appropriate for pore water at 100 C.

properties. Figure 3 shows preliminary results from one sample measured at room temperature with water from well J-13 at Yucca Mountain, Nevada as the pore fluid. This data was acquired using an automatic network analyzer to measure the transmission and reflection coefficients of a tuff sample machined to fit in an air line and from these the sample permittivity was calculated.<sup>3</sup> These data show a nearly linear, monotonically increasing relation between water content and dielectric permittivity at 200 MHz. Because we can only measure changes in electromagnetic properties, the slope of the least squares fit will be used to infer changes in rockmass water content. This data implies a 3.4% by volume change in water content per unit change in relative permittivity.

We will now consider an electromagnetic model for rock that will be useful for estimating the properties of tuff above

room temperature. The rock is considered a mixture of components, each having a specific electromagnetic property. To model an unsaturated rock we consider a three component mixture: solid matrix, pore water, pore air. Various theories, each with its characteristic approximations and assumptions, have been developed for such a dielectric mixture. Sihvola and Kong<sup>4</sup> review some of these theories. We will use a multiphase formula where the  $n$  different inclusion phases are in the form of arbitrary ellipsoids. If the inclusion orientations are random so that the mixture is isotropic on a macroscopic scale, the effective permittivity is

$$\epsilon_{eff} = \epsilon + \frac{\frac{1}{3} \sum_{j=1}^n f_j (\epsilon_j - \epsilon) \sum_{i=1}^3 \frac{\epsilon}{\epsilon + N_{ji} (\epsilon_j - \epsilon)}}{1 - \frac{1}{3} \sum_{j=1}^n f_j (\epsilon_j - \epsilon) \sum_{i=1}^3 \frac{N_{ji}}{\epsilon + N_{ji} (\epsilon_j - \epsilon)}} \quad (4)$$

where  $N_{ji}$ ,  $N_{ji}$ , and  $N_{ji}$  are the depolarization factors of the  $j^{\text{th}}$  phase,  $f_j = n_j v_j$  is the fractional volume of the  $j^{\text{th}}$  phase and  $\epsilon$  is the background permittivity. In our model the background dielectric is the silicate matrix and the two inclusion phases are the two pore fluids in a partially saturated rock—water and air. If the permittivities are complex, we have a model of a lossy mixture since  $\epsilon = \epsilon' - j\epsilon''$ , where ( $j = \sqrt{-1}$ ) and  $\epsilon' = \sigma/\omega\epsilon_0$ . The real component  $\epsilon'$  describes the phase velocity which is approximately  $V/\sqrt{\epsilon'}$ . The imaginary component describes energy dissipation from both dielectric (e.g., orientation of dipole moments) and ohmic losses (e.g., motion of charge carriers). Therefore,  $\sigma$  contains both dielectric and the more familiar ohmic conductivity. The angular frequency is  $\omega$ . Notice that the assumption of noninteracting inclusions is not really valid. That is, the inclusions are not isolated so that their perturbations on the field are independent. The effect of this on the calculated effective permittivity is not known. Unfortunately, we know of no mixture theory capable of accounting for interacting inclusions.

For our dielectric mixture model we need the permittivity of each component. The relative permittivity of water is known to be a very nearly constant value of 81.2 (at 17 C) between 0 and 600 MHz.<sup>5</sup> To demonstrate the use of Eq. (4) we assume  $\epsilon_1 = \epsilon_{\text{water}} = 80$  and  $\epsilon_2 = \epsilon_{\text{air}} = 1$ . To obtain the permittivity of the rock matrix, ( $\epsilon$  in Eq. (4)), we use our 200 MHz laboratory measurements of the dielectric permittivity of G-tunnel tuff (see Fig. 3). An automatic network analyzer was used to measure the transmission and reflection coefficients of a tuff sample machined to fit in an air line and from these the sample permittivity was calculated.<sup>1</sup> When the sample was dry, the calculated relative permittivity was 4.35. This value is not representative of the silicate matrix because it incorporates the effects of the 14 volume percent pore space. To calculate the silicate permittivity we can use Eq. (4) with  $\epsilon_{\text{eff}} = 4.35$  and solve for  $\epsilon$ . We model the rock as a single inclusion mixture; the pores as spherical inclusions ( $N_{ji} = N_{ji}$

$= N_{ji} = 1/3$ ) of volume fraction  $f = 0.14$  and  $\epsilon_1 = 1$  for air. We find that the silicate matrix relative permittivity is about 5.

Now, using the background permittivity  $\epsilon = 5$  in Eq. (4), we can estimate the rock permittivity as a function of porosity and saturation. Figure 3 shows the model results assuming the air component are spherical inclusions and the water component are randomly oriented thin needles (prolate spheroids, depolarization factors 0, 1/2, 1/2). This model was chosen because it is a reasonable representation to the measured data and is also a reasonable model for water held by capillarity along the pore wall and air filling the remaining central part of the pore. (It turns out that the results do not differ more than 10% if we assume randomly oriented disk shaped inclusions [oblate spheroids with depolarization factors 1, 0, 0] to model the water.)

This model should represent the rock at about 20 C but does not account for the fact that the permittivity of many materials depends on temperature. We have measured the permittivity of dry tuff and found that it is independent of temperature between 20 and 70 C. We conclude from this that the silicate matrix and air inclusion components of our mixture do not require a temperature dependent model. However, the relative permittivity of water has a well documented temperature dependence given by Eisenberg and Kauzmann<sup>6</sup> as  $\epsilon_w = 87.740 - 0.4T + 9.398 \times 10^{-4}T^2 - 1.41 \times 10^{-6}T^3$  where  $T$  is in degrees Celsius. When this dependence is included for water in Eq. (4), the effective permittivity of the mixture decreases with temperature as shown in Fig. 3.

These models demonstrate several concepts important to interpreting the permittivity tomographs. First, over the range of parameters of interest, the permittivity is nearly linearly related to the water content. This fact can be used to interpret the alternate tomographs, using the slope of the curves to infer changes in water content. Second, the fractional volume of pore filled by air contributes very little to the rockmass permittivity. This is because the silicate matrix and especially the water have such high permittivities compared to that of air. In fact, for practical considerations, the contribution of the air could be neglected and the system could be modeled with a single inclusion (water) in the background (silicate). Third, the effect of temperature on the water permittivity could be important to accurate determination of water content. For a saturated porosity of 15 volume% at 100 C, the water content could be underestimated by about 20% using the room temperature model. Also,  $de_{\text{eff}}/df_{\text{w}}$  will decrease about 28% between room temperature and 100 C. Ignoring this effect when interpreting an alternate tomograph would lead to an overestimate in the amount of dehydration during heating. Therefore, we will use the airline data in Fig. 3,  $de_{\text{eff}}/df_{\text{w}} = 29$ , to interpret changes in rockmass moisture content at or near room temperature but will assume a 28% smaller slope to interpret changes in moisture at 100 C.

## RESULTS AND DISCUSSION

**Ray Data.** The data shown in Fig. 4 is the measured relative permittivity along rays for which the transmitter and receiver were at common depths in their respective boreholes. Each point is a measure of the right hand side of Eq. (1) divided by the ray path length. For example, the point at 11.0 m depth represents the average permittivity (as a function of time) for the rock along a line which connects the transmitter and receiver at 11.0 m depth. We present this data first because it is part of the input to the reconstruction algorithm. Of course in this format the spatial information generated by the reconstruction is absent, but the artifacts generated by the reconstruction are also absent so that quantitative interpretation of the results should be more reliable.

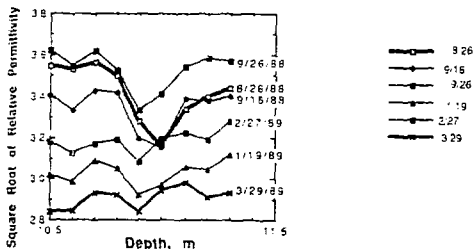


Figure 4. Measured square root of relative permittivity as a function of time, along rays for which the transmitter in Ne4 and receiver in Ne5 were at common depths. Each point is a measure of the right hand side of Eq. (1) divided by the ray path length.

Figure 4 shows an example of this data between Ne4 and Ne5. This plane is parallel to the heater, 0.75 m to one side and below the heater in elevation. Between August 26th, 1988 and March 29th, 1989 the relative permittivity decreased by approximately 3.8 (changes in  $\epsilon^{1/2}$  of about 0.5). Of course the rockmass is not homogeneous, therefore, this is a rough average over a region with extremes in permittivity changes from 4.5 to 1.8. If the rockmass was at 20°C during the period, a 3.8 variation would represent a change in fractional water content of about 0.13 (from the measured data in Fig. 3). If we assume the rockmass was always at 100°C the calculated water content change would be 28% higher or 0.17. The actual change in water content is likely between these values. Either figure represents a substantial drying of the rockmass at a distance of more than one meter from the end of the heater.

The overall dehydration measured between Ne4 and Ne5 appears not to be monotonic. The initial permittivity decrease was followed by an increase recorded on September 26th. This may correspond to a saturation halo preceding the drying front. If so the data indicate an increase in fractional moisture content up to 4.5 over initial conditions. The increase between January 19th and February 27th is of similar magnitude but both are of the order of the system calibration error and so that their interpretation is uncertain.

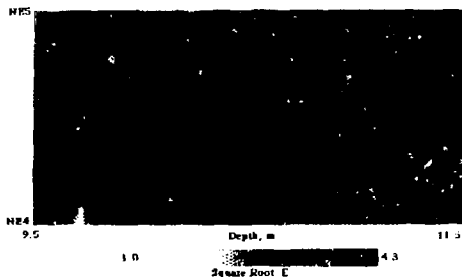
Cross borehole ray data between holes Ne2a to Ne6 and Ne6 to Ne7 (not shown here) indicate that before the experiment started there was a higher water content in the rockmass below the heater than above. These two data sets are from the uppermost and lowest parts of the rock where HFEM measurements were made. Because of the proximity of the heater to Ne6, data from the full length of that hole cannot be used for reliable calculation of permittivity values. However, data at the extremes of the range measured show that above the heater (between Ne6 and Ne7) the typical relative permittivity is about 7.8 while below the heater (between Ne2a and Ne6) the permittivity is typically about 10.0 (remember that these absolute values are not accurate because of uncertainties in system calibration but their relative magnitudes should be reliable). If these data are representative of the rockmass adjacent to the experiment, the upper part of the rock may be dryer than that below (lower fractional water content of 0.08). We have no way of knowing if this was a pristine condition. On the other hand, a possible external source of such a moisture gradient is the drill water used for the 11 boreholes used in the experiment.

**Tomographs.** Over the course of the 10 month experiment, data was acquired for more than 100 tomographs; each data set required the collecting of from 81 to 441 individual data points, depending on the region sampled. Figure 5 shows an example of the tomographs taken during the experiment for the region between boreholes Ne4 and Ne5 between 9.5 and 11.5 m depth. Unfortunately, the data used for these reconstructions was influenced by the proximity of this plane to the heater. However, we have determined that between 10.5 and 11.5 m the reconstructed  $\sqrt{\epsilon}$  is changed by less than 0.15 by the proximity of the heater. Shallower than 10.5 m the influence can be larger but varies a lot depending on the location within the image. Deeper than 10.5 m the reconstruction reflects more accurately, the heterogeneity in the rockmass permittivity before heating began. For this part of the image plane the variation in  $\epsilon^{1/2}$  introduced by measurement imprecision is 0.04 (estimated by comparing two tomographs taken when no known changes were occurring in the rockmass).<sup>1</sup>

Figure 5a is the tomograph between Ne4 and Ne5 before heating. The range of imaged relative permittivity deeper than 10.5 m is from about 6.2 to 16.0. The calibration data in Fig.

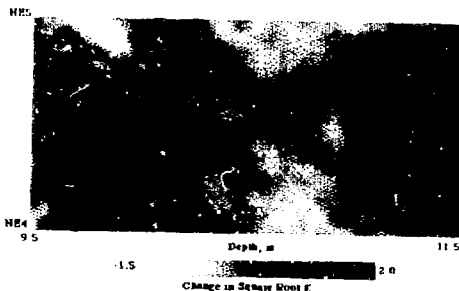
3 (extrapolated) suggests that this represents a fractional moisture content contrast of about 0.34. This is a fairly large range and is possible for only two small regions, each represented by a single pixel. A more representative range of permittivity is 9.0 to 12.2 which implies a contrast of 0.11 in fractional water content.

In this same reconstruction, the region near Ne4, at about 960 cm depth, is imaged as a very low permittivity. Even though this data is contaminated by the presence of the heater, our tests indicate that this anomaly is indicative of a rockmass anomaly. This region is likely a highly fractured zone with apertures too large to retain a significant amount of water by capillarity. The preheating borehole logging identified a highly fractured zone exactly at this location in Ne4. Typically, fracture orientation was measured in these logs. At this location, however, orientation could not be determined because of the high fracture density. An interesting speculation is that a particularly high porosity was created during drilling as a washout in an intensely broken zone. For the image plane as a whole, however, there seems to be a poor correlation between logged fractures in either borehole and either high or low permittivity image anomalies.



(a) Baseline image of  $(\epsilon_r)^{1/2}$  taken before the heater was turned on, August 26, 1988. Fractures and approximate orientation are shown as logged in both boreholes before the test began. The approximate location of the heater and borehole are projected into the image plane.

The alterant image at the end of the heating phase is shown in Fig. 5b. (The ramp down in heater power started January 13, 1989.) This image is formed as a pixel by pixel difference between the image for January 9 and the baseline data (Fig. 5a) such that positive values reflect an increase in permittivity with time. Much of the imaged structure between 9.5 and 10.5 m is contaminated by the heater interference. However, the strong positive anomaly at 9.6 m, earlier identified with a broken broken zone in Ne4, is probably real. This



(b) Alterant image of  $\Delta(\epsilon_r)^{1/2}$  for January 9, 1989. The color scale represents the change in  $(\epsilon_r)^{1/2}$  calculated by subtracting the baseline tomograph from the January 9th image so that an increase in permittivity is positive in the alterant image. Each image area is 2 m by 1.5 m, contains 416 pixels (each about 9 cm by 8 cm) and is reconstructed from phase measurements along approximately 440 ray paths.

Figure 5. Tomographs between Ne4 and Ne5 from 9.5 to 11.5 m depth.

positive anomaly persists throughout the heating period. If real, it means that the fracture zone intersecting Ne4 at this location is wetter than its preheating state throughout heating. This may be a highly conductive fracture zone that is draining condensate from the saturation halo to the rockmass below where it is lost to the system. Model calculations<sup>3</sup> indicate that if the matrix porosity in this zone is sufficiently high (assuming the capillary tension data used in the model is appropriate) then a significant flux of liquid water is unlikely in this fracture system. Liquid water may flow in the fractures if the fracture porosity is sufficiently large relatively to the matrix porosity and if the capillary tension data used in the hydrothermal scoping calculation<sup>4</sup> is not representative of this rock.

Deeper than 10.5 m the image is more reliable. As in the baseline image, there is no strong correlation of image anomalies with borehole fractures. This means that these fractures are neither wetter (acting as a flow path for liquid water) or dryer than the surrounding rock and perhaps contribute little to the hydrology of the system.

One puzzling property of the alterant tomograph of Fig. 5b is the high correlation between increases in permittivity during heating and regions of higher preheating rockmass permittivity. Conversely, regions of decreased permittivity correlate with regions of lower preheating permittivity. More specifically, while there is an overall decrease in permittivity during heating, the local regions that do indicate a small increase are those regions that have lower permittivity prior to heating. One possible explanation is that these are fractured zones; drained of water before the test, they contain condensate during heating.

**Summary.** HFEM data is useful for characterizing the water distribution in the near field of a simulated waste container. First, we used data from individual ray paths to determine quantitative estimates of how moisture content in the rockmass changes during heating. This interpretation is an average over the ray length between the boreholes so has little information on spatial variability. However, the results are semiquantitative; only with a valid calibration of the measurement system could the results be quantitatively reliable. With such a quantitative measurement, a determination of absolute water content of the rockmass may be possible. Second, we used the tomographs generated from the cross borehole data to infer properties of the spatial variability of water distribution. This interpretation lead to conclusions about the role of fractures in the system.

We have shown that the parallel scan data and the tomographs suggest that the rock immediately around the heater begins to dry as soon as the heater is turned on. Rock further from the heater shows an early wetting episode probably caused by condensation of steam in cooler portions of the rock. Following this wetting, the rock begins to dry as temperatures and evaporation rate increase. Some fractures and highly fractured zones may remain wetter than preheating conditions long after the surrounding rock matrix has begun dehydration. Our data does not directly indicate if this water is stationary or flowing. However, since other parts of the rockmass in these image planes are drying and these fractures are not, it is likely that these fractures are conduits for water movement during the heating process.

**Acknowledgements.** The authors are thankful for helpful discussions with J. Berryman, D. Wilder, and T. Buscheck. J. Beatty, D. Watwood, and J. Carbino provided valuable technical support.

## REFERENCES

1. W. D. DAILY and A. L. RAMIREZ, "Evaluation of Electromagnetic Tomography to Map *In Situ* Water in Heated Welded Tuff," *Water Resources Res.*, 25, no.6, 1083-1096, 1989.
2. K. A. DINES and R. J. LYTLE, "Computed Geophysical Tomography," *Proc. IEEE*, 67,1065-1073, 1979.
3. M. S. FREEMAN, R. N. NOTTENBURG, and J. B. DUBOW, "An Automated Frequency Domain Technique for Dielectric Spectroscopy of Materials," *J. Phys. E.: Sci. Instrum.*, 12, 899-903, 1979.
4. A. H. SIHVOLA and J. A. KONG, "Effective Permittivity of Dielectric Mixtures," *IEEE, Trans. on Geosci. and Remote Sensing*, 26, No. 4, 420-429, 1988.
5. N. E. DORSEY, "Properties of Ordinary Water-Substance," *American Chemical Society Monograph Series*, Hafner Publishing Co., NY, 1968.
6. D. EISENBERG and W. KAUZMANN, *The Structure and Properties of Water*, Oxford University Press, NY, 1969.
7. J. NITAO and T. A. BUSCHECK, "Asymptotic Behavior of a Liquid Front in an Unsaturated Fractured Porous Medium," to be submitted to *J. Amer. Nuclear Soc.*, 1989.
8. A. RAMIREZ and D. WILDER (eds.), "Prototype Engineered Barrier System Field Test (PEBSFT)—Progress Report through November 1, 1988," Lawrence Livermore National Laboratory UCID-21640, Livermore, CA, May 1989.